

Hollow CeO₂@Co₂N Nanosheets Derived from Co-ZIF-L for Boosting the Oxygen Evolution Reaction

Jian Zhang, Wenhui He, Harshitha Barike Aiyappa, Thomas Quast, Stefan Dieckhöfer, Denis Öhl, João R. C. Junqueira, Yen-Ting Chen, Justus Masa, and Wolfgang Schuhmann*

Rational design of highly active electrocatalysts for the oxygen evolution reaction (OER) is critical to improving overall electrochemical water splitting efficiency. This study suggests hollow CeO₂@Co₂N nanosheets synthesized using Co-ZIF-L as a precursor, followed by a hydrothermal reaction and a nitridation process as very attractive OER catalysts. The increased activity is supposed to be due to nitridation and strong electronic interaction between CeO₂ and Co₂N that contribute to the formation of active CoOOH phase. The synthesized CeO₂@Co₂N exhibits low overpotentials of 219 and 345 mV at OER current densities of 10 and 100 mA cm⁻², respectively, as well as a long-term durability of 30 h at a comparatively high current density of 100 mA cm⁻².

desired current densities.^[3] However, since the commonly used benchmark current density of ≥ 10 mA cm⁻² is about two orders of magnitude lower than that required for industrial applications, extensive efforts have been dedicated to developing highly efficient OER electrocatalysts.^[2,4] Currently, noble metal oxides such as IrO₂ and RuO₂ remain the state-of-the-art electrocatalysts for the OER.^[5] Owing to their scarcity and high cost, more attentions have been paid to explore earth-abundant first-row (3d) transition-metal elements like Fe-, Co, and Ni-based borides,^[6] sulfides,^[7] phosphides,^[8] and oxides.^[9] The active nature of these transition-metal composites has been

1. Introduction

Electrochemical water splitting powered by renewable electricity has been regarded as a promising technology to sustainably generate hydrogen.^[1,2] However, the crucial limitation of water-splitting technologies is the anodic oxygen evolution reaction (OER), in which a substantial overpotential is required to overcome the sluggish four-electron/four-proton process for achieving the


intensively investigated, and in situ reconstruction of these composites into metal oxyhydroxides with high metal oxidation states has been recognized as a key to reach high catalytic activity.^[10] Although the mechanism of this reconstruction process has not been well elucidated so far, a series of strategies, such as the design of multi-metal composites^[11] or tuning the types of anionic ligands coordinating to the metal centers^[12] were suggested to accelerate this process and stabilize the formed active sites. However, due to the complexity of this reconstruction process, expediting the formation and maximum exposure of active metal oxyhydroxides on these metal composites remains a great challenge, which is critical for further boosting their O₂-evolution activity.

Zeolitic imidazolate frameworks (ZIF) derived by connecting metal ions with organic linkers have been widely used as metal-ion sources or template for synthesizing high-efficient catalysts.^[13] The instability of ZIF coordination structures upon exposure of the material to a variety of physical or chemical stimulations such as UV light, solvothermal treatment, or pH variations enables slow and controllable release of metal ions and linkers, which provides an ideal platform for the formation of active catalysts comprising a functional hybrid nanostructure.^[14] CeO₂ has been intensively employed as co-catalysts to activate various metal oxides,^[15,16] sulfides,^[17,18] and hydroxides^[19] (e.g., CoO_x and NiFe hydroxides) towards the HER or the OER. Under OER conditions, the redox transition of Ce³⁺ to Ce⁴⁺ may lead to the formation of oxygen vacancies, which act as Lewis acid sites facilitating the activation of H₂O molecules as a Lewis base.^[19] Additionally, strong electronic interaction between CeO₂ and the metal composites may modulate the adsorption strength of oxygen intermediates on the metal centers, finally accelerating the OER kinetics.^[16,20,21]

J. Zhang, Dr. W. He, Dr. H. B. Aiyappa, T. Quast, S. Dieckhöfer, Dr. D. Öhl, J. R. C. Junqueira, Prof. W. Schuhmann
Analytical Chemistry—Center for Electrochemical Sciences (CES)
Faculty of Chemistry and Biochemistry
Ruhr University Bochum
Universitätsstr. 150, D-44780 Bochum, Germany
E-mail: wolfgang.schuhmann@rub.de

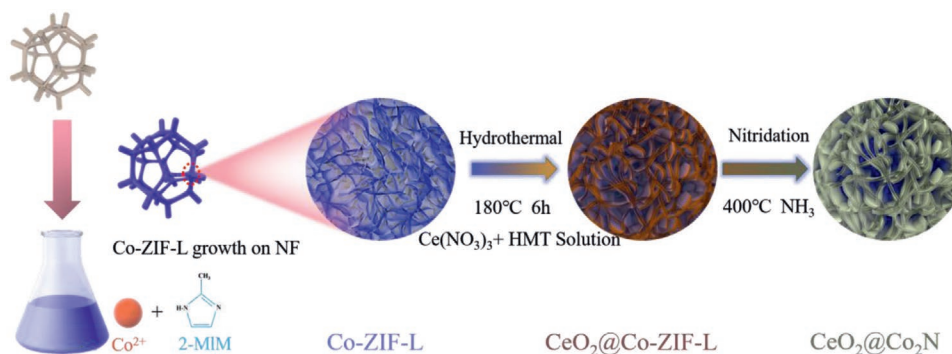
Dr. Y.-T. Chen
Center for Solvation Science (ZEMOS)
Ruhr University Bochum
D-44801 Bochum, Germany

Dr. J. Masa
Department of Heterogeneous Reactions
Max Planck Institute for Chemical Energy Conversion
Stiftstrasse 34-36, D-45470 Mülheim an der Ruhr, Germany

 The ORCID identification number(s) for the author(s) of this article can be found under <https://doi.org/10.1002/admi.202100041>.

© 2021 The Authors. Advanced Materials Interfaces published by Wiley-VCH GmbH. This is an open access article under the terms of the Creative Commons Attribution-NonCommercial-NoDerivs License, which permits use and distribution in any medium, provided the original work is properly cited, the use is non-commercial and no modifications or adaptations are made.

DOI: 10.1002/admi.202100041



Scheme 1. Schematic illustration of the synthesis of $\text{CeO}_2@Co_2N$.

Based on these considerations, the development of efficient pathways to exert synergistic effects between CeO_2 and metal composites, while maximizing the exposure of the active metal oxyhydroxide species, is a rational means to modulate OER activity. We developed a nanostructured $Co_2N@CeO_2$ composite material with rich nanoscale phase boundaries by utilizing the self-templating effect of ZIF. In an initial solvothermal process, the gradual degradation of Co-ZIF-L combined with slow hydrolysis of Ce^{3+} ions generates uniform mixed phases of CoO_x and CeO_2 . In a subsequent nitridation process, CoO_x is converted into Co_2N nanocrystals. At the same time, the strong interplay between Co_2N and CeO_2 leads to the formation of closely interconnected hollow networks. This unique structure of the $\text{Co}_2N/\text{CeO}_2$ hybrids provides a large accessible surface exposing the active catalytic sites. Electrochemical characterization and in situ Raman spectroscopy demonstrated excellent OER activity of the obtained $\text{Co}_2N/\text{CeO}_2$ hybrid material due to reconstruction of the Co_2N nanocrystals into cobalt oxyhydroxides, which enables an OER current density of 10 and 100 mA cm^{-2} at low overpotentials of only 219 and 345 mV, respectively.

2. Results and Discussion

The synthesis route of $\text{CeO}_2@Co_2N$ is illustrated by **Scheme 1**. In the first step, the precursor Co-ZIF-L nanosheets were uniformly deposited by immersing Ni foam into a solution of cobalt nitrate and 2-methylimidazole (2-MIM) at room temperature (**Figure 1a**; **Figure S1**, Supporting Information). The corresponding SEM images (**Figure 1b**; **Figure S2a–c**, Supporting Information) show that during hydrothermal treatment (in a $\text{Ce}(\text{NO}_3)_3 \cdot 6\text{H}_2\text{O}$ and HMT solution), the Co-ZIF-L precursor is converted into $\text{CeO}_2@Co\text{-ZIF-L}$ hollow nanosheets that are caused by an etching process involving hydrolysis of Co^{2+} and oxidation of Ce^{3+} .^[22]

The formation of the hollow nanostructure can further be confirmed by means of scanning transmission electron microscopy (STEM) (**Figure S3d**, Supporting Information), and is supposedly advantageous for the mass transport and the exposure of active sites. Energy-dispersive X-ray (EDX) elemental mapping (**Figure S3e**, Supporting Information) further indicated homogeneous distribution of Ce, Co, O, and N. High-resolution TEM (HR-TEM) images (**Figure S3b,c**, Supporting Information) of $\text{CeO}_2@Co\text{-ZIF-L}$ only show the well-resolved lattice fringes of the CeO_2 phase due to the fact

that Co-ZIF-L is amorphous. This result is corroborated by the selected area electron diffraction (SAED) pattern (**Figure S3a** inset and **Table S1**, Supporting Information). The observed bright rings are only indexed to the CeO_2 phase. Subsequently, the $\text{CeO}_2@Co\text{-ZIF-L}$ was converted into $\text{CeO}_2@Co_2N$ under NH_3 atmosphere at 400 °C. The well-distributed hollow nanosheets were maintained after the nitridation process (SEM image in **Figure 1c**; **Figure S2d–f**, Supporting Information), and the STEM images in **Figure 1g** further reveal the existence of the hollow nanosheets. EDX elemental mapping (**Figure 1h**) was employed to determine the elemental distribution of $\text{CeO}_2@Co_2N$, which shows a coexistence and the uniform distribution of Ce, Co, O, and N in the hollow nanohybrid material. The HR-TEM image (**Figure 1e,f**) of $\text{CeO}_2@Co_2N$ shows lattice fringes with the interplanar spacings of ≈ 2.15 and ≈ 2.46 Å, which correspond to the (111) and (110) plane of Co_2N . Interplanar spacing of ≈ 2.70 and ≈ 1.93 Å was also observed from the HR-TEM image, consistent with the values for the CeO_2 (200) and CeO_2 (220). More importantly, the rich nanoscale interface between Co_2N and CeO_2 can be observed in the HR-TEM images that indicate the close connection between the constituent phases. The observed ring in the SAED pattern (**Figure 1b** inset; **Table S1**, Supporting Information) can be indexed to the (002) planes of Co_2N as well as the (111), (200), and (220) planes of CeO_2 , revealing the hybrid and polycrystalline nature of $\text{CeO}_2@Co_2N$.

The chemical states and elemental bonding configuration in the surface region of $\text{CeO}_2@Co_2N$ were analyzed by means of X-ray photoelectron spectroscopy (XPS). As shown in the high-resolution XP spectra (**Figure 2**), $\text{CeO}_2@Co_2N$ as expected is composed of Ce, Co, N, and O. The Ce 3d high-resolution XP spectrum (**Figure 2a**) shows peaks at 878–899 and 900–920 eV corresponding to the Ce 3d 5/2 and Ce 3d 3/2 doublets of different components and their corresponding satellite peaks, which reveals the coexistence of Ce^{4+} and Ce^{3+} . The Ce 3d 5/2 peaks at 882.10 and 884.05 eV are assigned to Ce^{4+} and Ce^{3+} . The molar ratio of Ce^{4+} to Ce^{3+} is related to the amount of oxygen vacancies, which influences the catalytic OER performance.^[15,20,23]

The 3/2 branch in the Co 2p spectrum in **Figure 2b** shows three peaks corresponding to Co^{2+} and the Co^{2+} satellite, including $\text{Co}^{2+}\text{-O}$ (780.48 eV) and $\text{Co}^{2+}\text{-N}$ (782.80 eV).^[24,25] In **Figure 2c**, the N 1s spectrum of $\text{CeO}_2@Co_2N$ shows three peaks at 398.10, 399.06, and 400.56 eV, corresponding to pyridinic N, Co–N, and pyrrolic N, respectively.^[26] The peaks at

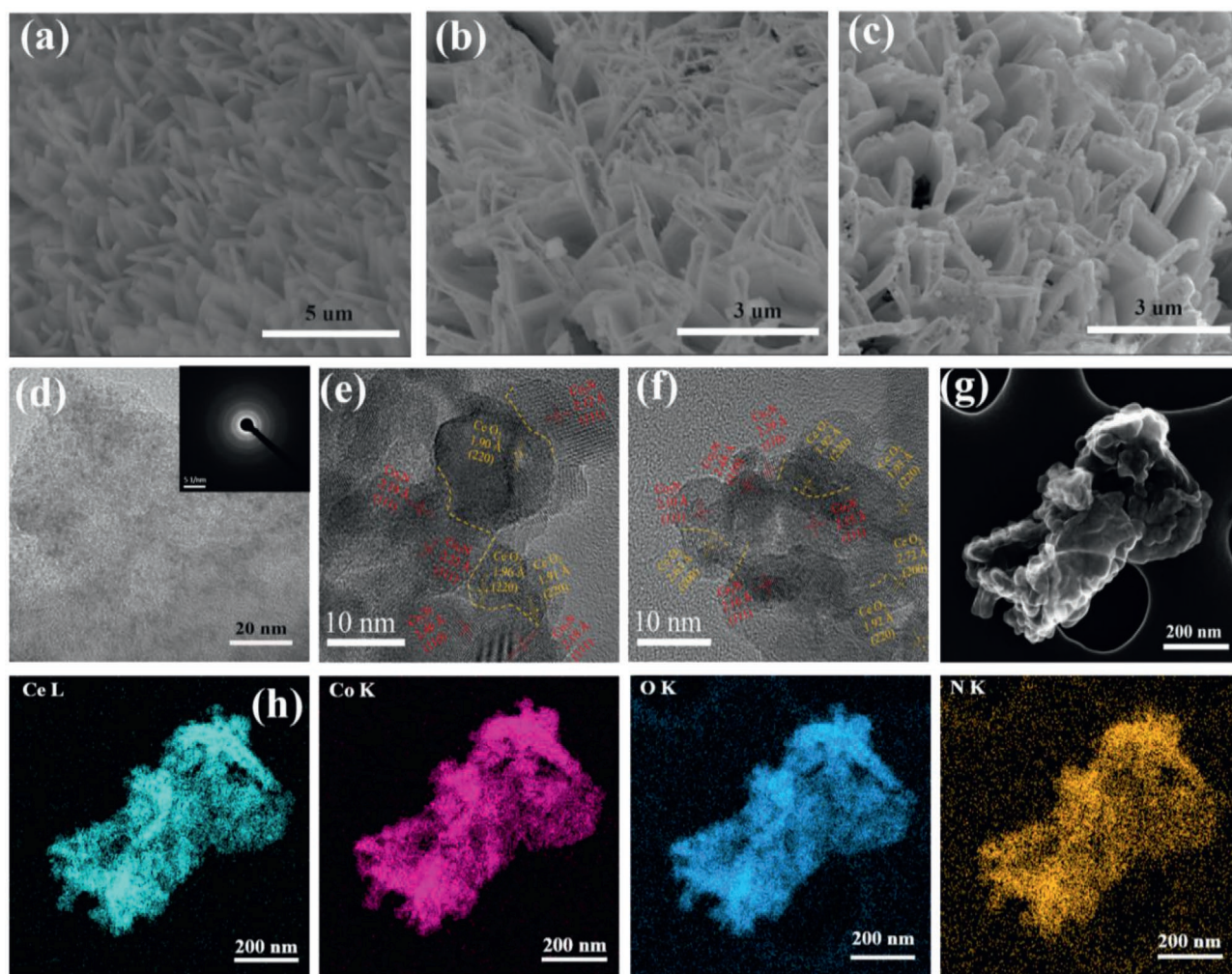


Figure 1. a–c) SEM images of Co-ZIF-L, CeO₂@Co-ZIF-L, and CeO₂@Co₂N. d) TEM images of CeO₂@Co₂N. The inset shows the SAED pattern. e, f) HR-TEM images of CeO₂@Co₂N. g) STEM image of CeO₂@Co₂N. h) EDX elemental mapping of CeO₂@Co₂N.

529.03, 530.19, 531.28, and 533.46 eV in the high-resolution XP spectrum of O 1s (Figure 2d) can be assigned to Ce–O, Co–O, O–H bond, and absorbed water, respectively.^[24,27]

To explore the OER performance of the obtained CeO₂@Co₂N nanosheets, we compared their OER performance with that of CeO₂@Co-ZIF-L with different amounts of Ce (Figure S7a, Supporting Information); the CeO₂@Co-ZIF-L with the second lowest loading of Ce(NO₃)₃ (0.0025 mmol Ce(NO₃)₃) exhibited the highest OER performance. After nitridation, the formed CeO₂@Co₂N (0.0025 mmol Ce(NO₃)₃) retained the lowest overpotential as compared with other CeO₂@Co₂N materials containing different amounts of Ce (Figure S7b, Supporting Information).

The samples with the highest OER activity, denoted as CeO₂@Co₂N, will be discussed in more detail in the following. As shown in **Figure 3a**, linear sweep voltammetry (LSV) for CeO₂@Co₂N, CeO₂@Co-ZIF-L, Co–N (Co-ZIF-L after nitridation), CeO₂, and Ni foam was performed for comparison. The OER performance of CeO₂@Co₂N (219 mV at 10 mA cm⁻²) is clearly higher than the other samples at the same current density (Figure 3a inset). Noteworthy, CeO₂@Co₂N also exhibited the lowest overpotential of 345 and 375 mV to

achieve a current density of 100 and 200 mA cm⁻², respectively (Figure 3b). The superior OER performance of CeO₂@Co₂N was also confirmed by comparison with the performance of the state-of-the-art benchmark catalyst RuO₂ (Figure S8, Supporting Information). Electrochemical RuO₂ data obtained under the same experimental conditions revealed that CeO₂@Co₂N has a lower overpotential at all current densities compared to RuO₂ deposited on Ni foam. Tafel plots derived from the linear sweep voltammograms were used to evaluate the OER kinetics for the different catalysts (Figure 3c). The Tafel slope for the CeO₂@Co₂N is 95.8 mV dec⁻¹, which is similar to that of CeO₂@Co-ZIF-L (98.7 mV dec⁻¹), and lower than that of Co–N (120.1 mV dec⁻¹) and CeO₂ (139.2 mV dec⁻¹), indicating improved OER kinetics. The stability of the CeO₂@Co₂N was investigated by means of long-term chronopotentiometry. As shown in Figure 3d, the OER activity was maintained for at least 30 h at a current density of 100 mA cm⁻², while the hollow nanosheet morphology was preserved (Figure S4, Supporting Information). EDX elemental mapping images show that the constituting elements are still uniformly distributed within the nanosheet structure after the long-term experiment

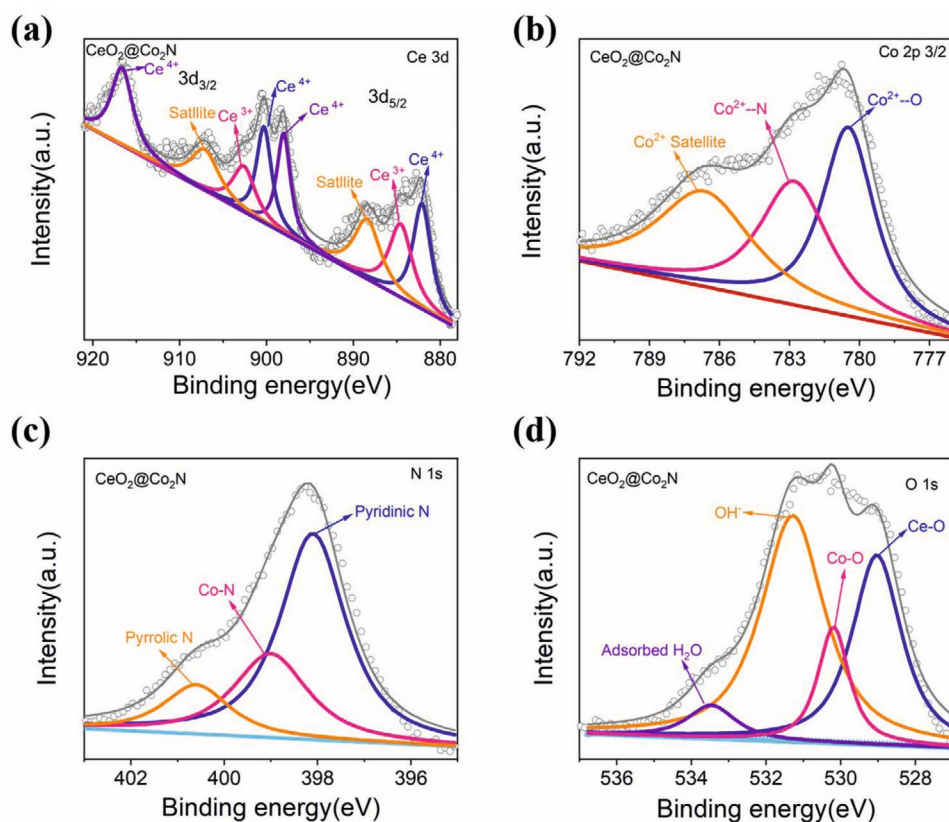


Figure 2. High-resolution XPS spectra of a) Ce 3d, b) Co 2p 3/2, c) N 1s, and d) O 1s.

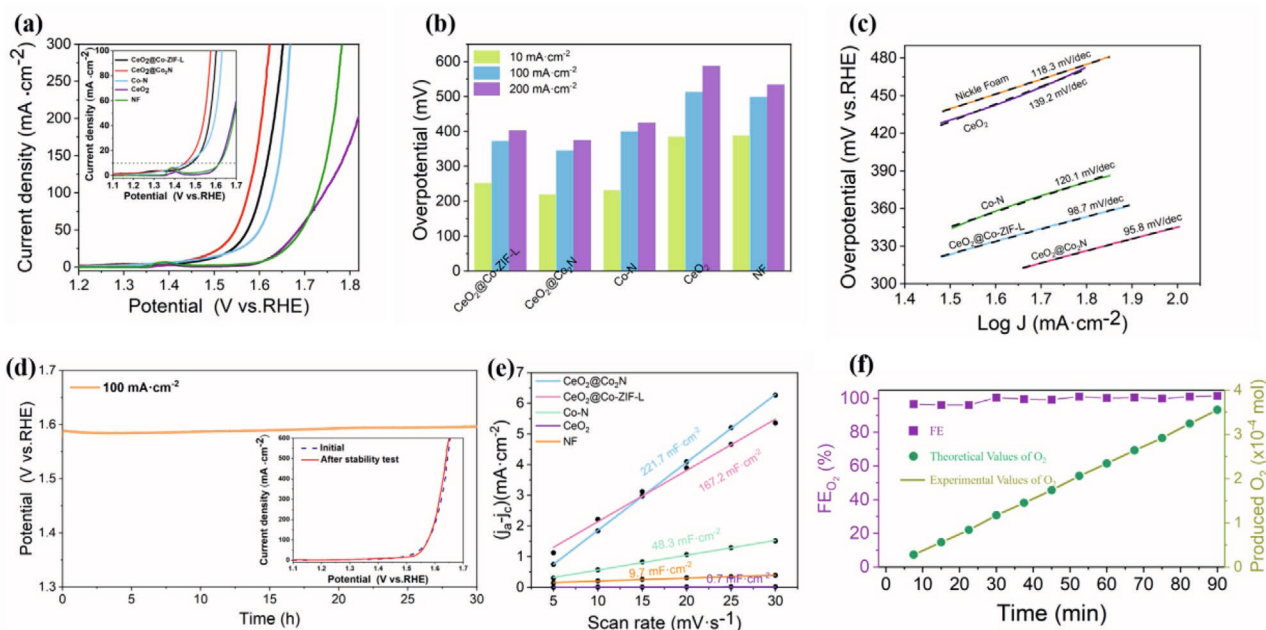


Figure 3. a) LSV polarization curves of $\text{CeO}_2@Co_2N$, $\text{CeO}_2@Co-ZIF-L$, $Co-N$, Co_2O_3 , and Ni foam in purified 1 M KOH as electrolyte. b) Bar graph of the overpotential at current densities of 10, 100, and 200 mA cm^{-2} for $\text{CeO}_2@Co_2N$, $\text{CeO}_2@Co-ZIF-L$, $Co-N$, Co_2O_3 , and Ni foam. c) Tafel plots of $\text{CeO}_2@Co_2N$, $\text{CeO}_2@Co-ZIF-L$, $Co-N$, Co_2O_3 , and Ni foam. d) Chronopotentiometric stability test of $\text{CeO}_2@Co_2N$ at a current density of 100 mA cm^{-2} . e) Scan-rate-dependent capacitive currents for $\text{CeO}_2@Co_2N$, $\text{CeO}_2@Co-ZIF-L$, $Co-N$, NF, and Co_2O_3 . f) Amount of O_2 theoretically calculated and experimentally measured and Faradaic efficiency versus time for $\text{CeO}_2@Co_2N$ during OER.

(Figure S5d,e, Supporting Information). As shown in the elemental composition of $\text{CeO}_2@\text{Co}_2\text{N}$ before and after stability test (Figure S6 inset, Supporting Information), the molar ratio of Ce to Co remains unchanged after the stability test, which further indicate the favorable electrochemical stability of $\text{CeO}_2@\text{Co}_2\text{N}$ during polarization to high current densities. In TEM-EDS (Figure S6 inset, Supporting Information), we did not detect any Ni peaks in $\text{CeO}_2@\text{Co}_2\text{N}$ before and after stability test, which indicated that the Ni foam support does not contribute to electrocatalysis. From HR-TEM images and SAED measurements of $\text{CeO}_2@\text{Co}_2\text{N}$ after the stability test, it can be inferred that only crystal phases of CeO_2 are detected due to the conversion of the Co_2N nanocrystals into amorphous cobalt oxide and oxyhydroxides during the stability test (Figure S5a–c and Table S1, Supporting Information). $\text{CeO}_2@\text{Co}_2\text{N}$ with a hollow nanosheet structure exhibits superior catalytic performance for the OER in terms of both activity and stability. In

fact, as shown in Table S2, Supporting Information, both the overpotential and stability of $\text{CeO}_2@\text{Co}_2\text{N}$ are superior to the reported CeO_x series OER electrocatalysts. To understand the reasons behind the excellent catalytic performance for the OER, we compared the electrochemically active surface area (ECSA) of $\text{CeO}_2@\text{Co}_2\text{N}$, $\text{CeO}_2@\text{Co-ZIF-L}$, Co-N , CeO_2 , and Ni foam. In Figure 3e and Figure S9, Supporting Information, the double-layer capacitance (C_{dl}) of $\text{CeO}_2@\text{Co}_2\text{N}$ (221.7 mF cm^{-2}) and $\text{CeO}_2@\text{Co-ZIF-L}$ (167.2 mF cm^{-2}) were much larger than that of the other samples like Co-N (48.3 mF cm^{-2}), Ni foam (9.7 mF cm^{-2}), and CeO_2 (0.7 mF cm^{-2}) due to their unique hollow structure that is advantageous for the mass transport and the exposure of active sites. The further increased C_{dl} for $\text{CeO}_2@\text{Co}_2\text{N}$ compared with $\text{CeO}_2@\text{Co-ZIF-L}$ is indicating a higher number of exposed active sites generated during nitridation. The polarization curves of $\text{CeO}_2@\text{Co}_2\text{N}$ and $\text{CeO}_2@\text{Co-ZIF-L}$ were normalized by their corresponding C_{dl} values

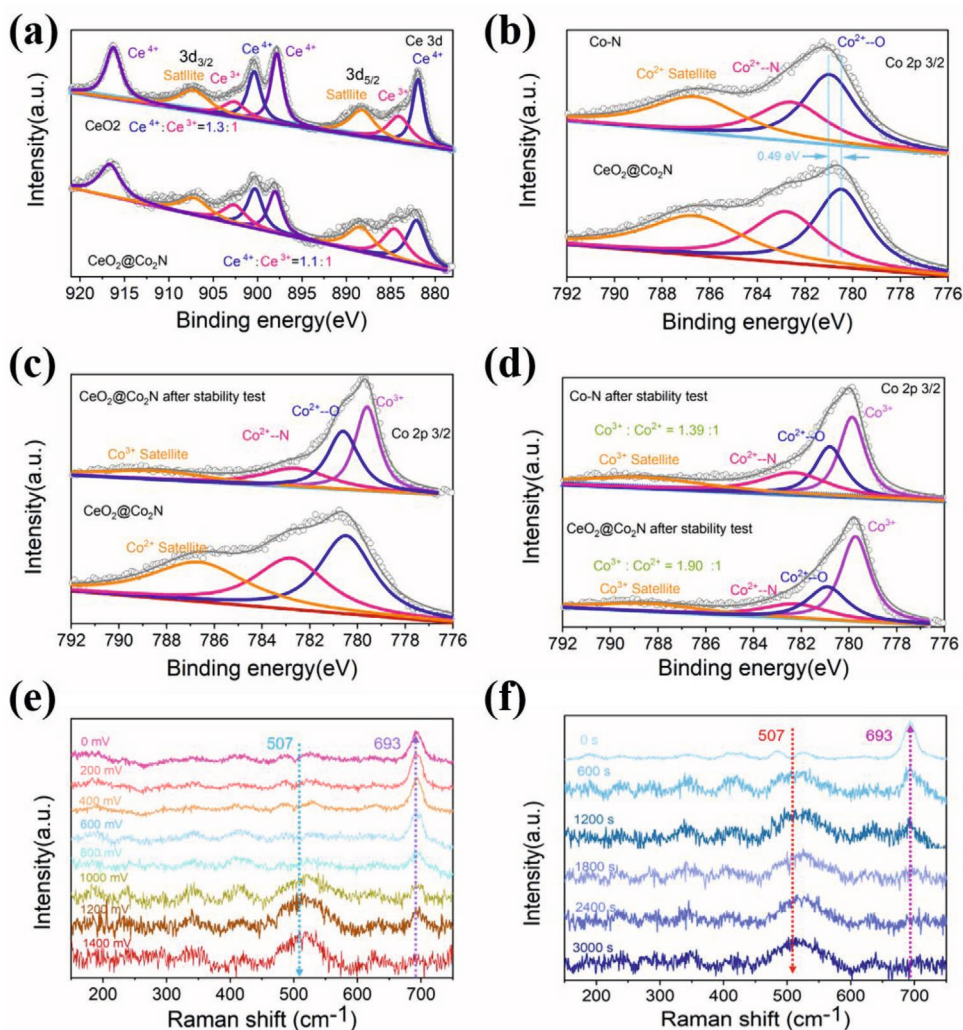


Figure 4. a) Ce 3d XPS spectra of $\text{CeO}_2@\text{Co}_2\text{N}$ and CeO_2 . b) Co 2p 3/2 XPS spectra of $\text{CeO}_2@\text{Co}_2\text{N}$ and Co-N . c) Co 2p 3/2 XPS spectra of $\text{CeO}_2@\text{Co}_2\text{N}$ and CeO_2 after the galvanostatic stability test for 30 h at a current density of 100 mA cm^{-2} . d) Co 2p 3/2 XPS spectra of Co-N and $\text{CeO}_2@\text{Co}_2\text{N}$ after the 30 h galvanostatic stability test at a current density of 100 mA cm^{-2} . e) In situ Raman spectroscopy study of $\text{CeO}_2@\text{Co}_2\text{N}$ in a potential range between 0 and 1400 mV in 0.01 M KOH (vs Ag/AgCl/3 M KCl). The sampling interval is 200 mV. f) In situ Raman spectra of $\text{CeO}_2@\text{Co}_2\text{N}$ at different durations during the amperometric treatment at 800 mV in 0.01 M KOH (vs Ag/AgCl/3 M KCl).

(Figure S10, Supporting Information) and the intrinsic activity of $\text{CeO}_2@\text{Co}_2\text{N}$ is higher than that of $\text{CeO}_2@\text{Co-ZIF-L}$. We conclude that the high electrocatalytic activity of $\text{CeO}_2@\text{Co}_2\text{N}$ mainly originated from its high intrinsic activity. In the Figure 3f, the amount of O_2 evolved during the OER from $\text{CeO}_2@\text{Co}_2\text{N}$ was determined quantitatively by gas chromatography. The amount of O_2 that was experimentally measured and theoretically calculated from the transferred charge is identical revealing the nearly 100% Faradaic efficiency for the OER using $\text{CeO}_2@\text{Co}_2\text{N}$ -modified electrodes.

To further understand the structure–performance relationships, XPS measurements were performed to study the chemical interaction between CeO_2 and Co_2N . Figure 4a illustrates the high-resolution XP spectrum of Ce 3d for CeO_2 and $\text{CeO}_2@\text{Co}_2\text{N}$. The $\text{Ce}^{4+}:\text{Ce}^{3+}$ molar ratio for CeO_2 is 1.3:1, while the value for $\text{CeO}_2@\text{Co}_2\text{N}$ decreases to 1.1:1. The number of oxygen vacancies is supposed to be correlated with ratio of Ce^{3+} to Ce^{4+} and is frequently measured by means of XPS. Hence, we suppose that the number of oxygen vacancies increased upon incorporating Co_2N that could improve the electronic conductivity and the number of active OER sites.^[17]

In the XP spectrum of Co 2p 3/2 for Co–N and $\text{CeO}_2@\text{Co}_2\text{N}$ (Figure 4b, the Co 2p 3/2 peak of $\text{Co}^{2+}-\text{O}$ (780.48 eV) in $\text{CeO}_2@\text{Co}_2\text{N}$ shows a 0.49 eV negative shift compared with that in Co–N, which indicates strong electronic interaction between CeO_2 and Co_2N . The binding energy of Co^{2+} is closer to the binding energy of Co^{3+} (CoOOH), which implies that it is easier for Co^{2+} ions to lose electrons and be converted to Co^{3+} (CoOOH) and this is the prerequisite for the formation of the catalytically active phase for the OER. Furthermore, the surface changes of $\text{CeO}_2@\text{Co}_2\text{N}$ after the stability test were investigated by XPS. In the XP spectrum of Ce 3d (Figure S11, Supporting Information), the $\text{Ce}^{4+}:\text{Ce}^{3+}$ molar ratio of $\text{CeO}_2@\text{Co}_2\text{N}$ did not significantly change (1.10:1 to 1.05:1), suggesting a high chemical surface stability of CeO_2 during the long-term measurement. As shown in Figure 4c, a new peak for Co^{3+} (CoOOH) at 779.56 eV can be observed after the stability test, which reveals the conversion of Co^{2+} to Co^{3+} (CoOOH). To further support the conclusion that it is easier in the case of $\text{CeO}_2@\text{Co}_2\text{N}$ to oxidize Co^{2+} to Co^{3+} (CoOOH), we compared XP spectra of Co 2p 3/2 of Co–N and $\text{CeO}_2@\text{Co}_2\text{N}$ after the stability test. As shown in the Figure 4d, the molar ratio of Co^{3+} to Co^{2+} for Co–N and $\text{CeO}_2@\text{Co}_2\text{N}$ is 1.39 and 1.90, respectively, which indicates that more of the active CoOOH phase is generated as compared with Co–N. Thus, the XPS results suggest that CeO_2 facilitates the formation of the active CoOOH phase. In situ Raman spectroscopy provides insights into the structural evolution during electrocatalysis. The region between 150 and 750 cm^{-1} reflecting the lattice vibrations of cobalt oxides and hydroxides is shown in Figure 4e,f and Figure S9, Supporting Information. Representative Raman peaks of CoO_x or $\text{Co}(\text{OH})_2$ at around 693, 621, 525, 483, and 193 cm^{-1} can be found in the sample of $\text{CeO}_2@\text{Co}_2\text{N}$ (Figure S9, Supporting Information).^[28] With increasing applied potential, the Raman peak intensity at 693 cm^{-1} decreased gradually, while a new peak starts to emerge at the 507 cm^{-1} at an applied potential 1000 mV (vs Ag/AgCl/3 M KCl), which is assigned to the formation of CoOOH .^[29] In contrast, in the in situ Raman spectrum of Co–N (Figure S13, Supporting Information), the peak for

CoOOH starts to appear only at an applied potential of 1200 mV (vs Ag/AgCl/3 M KCl), which additionally suggests that the active CoOOH phase is easier formed in the case of $\text{CeO}_2@\text{Co}_2\text{N}$. The increased applied potential leads to the conversion of Co species to CoOOH that can be further confirmed when a potential of 800 mV (vs Ag/AgCl 3 M KCl) was continuously applied. After 600 s, the formation of CoOOH was observed, while the intensity of the Raman peak of CoO_x decreased over time. These findings are supported by XPS as shown before.

3. Conclusion

In summary, a novel hybrid nanostructure consisting of hollow $\text{CeO}_2@\text{Co}_2\text{N}$ nanosheets derived from the Co-ZIF-L exhibits excellent performance towards the OER in alkaline electrolyte. The improved catalytic performance of $\text{CeO}_2@\text{Co}_2\text{N}$ is mainly due to 1) the increased number and accessibility of active sites upon nitridation and 2) the strong electronic interaction between CeO_2 and Co_2N that facilitates the formation of the active phase CoOOH . These results reveal that the $\text{CeO}_2@\text{Co}_2\text{N}$ nanosheets hold promise for application as an efficient non-noble OER electrocatalysts in terms of activity and stability.

Supporting Information

Supporting Information is available from the Wiley Online Library or from the author.

Acknowledgements

This research was funded by the Deutsche Forschungsgemeinschaft (DFG, German Research Foundation) within the collaborative research center/transregio 247 “Heterogeneous Oxidation Catalysis in the Liquid Phase” TRR 247 (388390466). The project received funding from the European Research Council (ERC) under the European Union’s Horizon 2020 research and innovation program (grant agreement CasCat (833408)). J.Z. acknowledges the Chinese Scholarship Council for a Ph.D. fellowship.

Open access funding enabled and organized by Projekt DEAL.

Conflict of Interest

The authors declare no conflict of interest.

Data Availability Statement

Research data are not shared.

Keywords

cerium oxides, cobalt nitride, electronic interactions, hollow nanosheets, non-noble-metal electrocatalysts, oxygen evolution reaction

Received: January 25, 2021
Published online: March 6, 2021

[1] a) X. Zou, Y. Zhang, *Chem. Soc. Rev.* **2015**, *44*, 5148; b) B. You, Y. Sun, *Acc. Chem. Res.* **2018**, *51*, 1571; c) S. Gupta, M. K. Patel, A. Miotello, N. Patel, *Adv. Funct. Mater.* **2020**, *30*, 1906481.

- [2] B. M. Hunter, H. B. Gray, A. M. Müller, *Chem. Rev.* **2016**, *116*, 14120.
- [3] a) S. Anantharaj, S. R. Ede, K. Sakthikumar, K. Karthick, S. Mishra, S. Kundu, *ACS Catal.* **2016**, *6*, 8069; b) Y. Liang, Y. Li, H. Wang, H. Dai, *J. Am. Chem. Soc.* **2013**, *135*, 2013; c) Z.-P. Wu, X. F. Lu, S.-Q. Zang, X. W. Lou, *Adv. Funct. Mater.* **2020**, *30*, 1910274.
- [4] M. Tahir, L. Pan, F. Idrees, X. Zhang, L. Wang, J.-J. Zou, Z. L. Wang, *Nano Energy* **2017**, *37*, 136.
- [5] a) R. Ge, L. Li, J. Su, Y. Lin, Z. Tian, L. Chen, *Adv. Energy Mater.* **2019**, *9*, 1901313; b) X. Liang, L. Shi, Y. Liu, H. Chen, R. Si, W. Yan, Q. Zhang, G.-D. Li, L. Yang, X. Zou, *Angew. Chem., Int. Ed.* **2019**, *58*, 7631.
- [6] a) J. Masa, I. Sinev, H. Mistry, E. Ventosa, M. de La Mata, J. Arbiol, M. Muhler, B. Roldan Cuenya, W. Schuhmann, *Adv. Energy Mater.* **2017**, *7*, 1700381; b) J. Masa, P. Weide, D. Peeters, I. Sinev, W. Xia, Z. Sun, C. Somsen, M. Muhler, W. Schuhmann, *Adv. Energy Mater.* **2016**, *6*, 1502313.
- [7] a) W. Chen, H. Wang, Y. Li, Y. Liu, J. Sun, S. Lee, J.-S. Lee, Y. Cui, *ACS Cent. Sci.* **2015**, *1*, 244; b) O. Mabayoje, A. Shoola, B. R. Wygant, C. B. Mullins, *ACS Energy Lett.* **2016**, *1*, 195; c) K. Jayaramulu, J. Masa, O. Tomanec, D. Peeters, V. Ranc, A. Schneemann, R. Zboril, W. Schuhmann, R. A. Fischer, *Adv. Funct. Mater.* **2017**, *27*, 1700451.
- [8] a) P. Wilde, S. Dieckhöfer, T. Quast, W. Xiang, A. Bhatt, Y.-T. Chen, S. Seisel, S. Barwe, C. Andronesco, T. Li, W. Schuhmann, J. Masa, *ACS Appl. Energy Mater.* **2020**, *3*, 2304; b) A. Dutta, A. K. Samantara, S. K. Dutta, B. K. Jena, N. Pradhan, *ACS Energy Lett.* **2016**, *1*, 169; c) A. Dutta, S. Mutyala, A. K. Samantara, S. Bera, B. K. Jena, N. Pradhan, *ACS Energy Lett.* **2018**, *3*, 141; d) B. Qiu, L. Cai, Y. Wang, Z. Lin, Y. Zuo, M. Wang, Y. Chai, *Adv. Funct. Mater.* **2018**, *28*, 1706008.
- [9] a) J. S. Kim, B. Kim, H. Kim, K. Kang, *Adv. Energy Mater.* **2018**, *8*, 1702774; b) J. He, B. Hu, Y. Zhao, *Adv. Funct. Mater.* **2016**, *26*, 5998.
- [10] a) D. Liu, H. Ai, J. Li, M. Fang, M. Chen, D. Liu, X. Du, P. Zhou, F. Li, K. H. Lo, Y. Tang, S. Chen, L. Wang, G. Xing, H. Pan, *Adv. Energy Mater.* **2020**, *10*, 2002464; b) L. Yu, Q. Zhu, S. Song, B. McElhenny, D. Wang, C. Wu, Z. Qin, J. Bao, Y. Yu, S. Chen, Z. Ren, *Nat. Commun.* **2019**, *10*, 5106; c) A. Bergmann, T. E. Jones, E. M. Moreno, D. Teschner, P. Chernev, M. Gliech, T. Reier, H. Dau, P. Strasser, *Nat. Catal.* **2018**, *1*, 711.
- [11] a) M. Chauhan, K. P. Reddy, C. S. Gopinath, S. Deka, *ACS Catal.* **2017**, *7*, 5871; b) J. Zhang, X. Li, Y. Liu, Z. Zeng, X. Cheng, Y. Wang, W. Tu, M. Pan, *Nanoscale* **2018**, *10*, 11997; c) H. Chen, S. Ouyang, M. Zhao, Y. Li, J. Ye, *ACS Appl. Mater. Interfaces* **2017**, *9*, 40333; d) B. Wang, K. Zhao, Z. Yu, C. Sun, Z. Wang, N. Feng, L. Mai, Y. Wang, Y. Xia, *Energy Environ. Sci.* **2020**, *13*, 2200.
- [12] a) W. He, H.-M. Gao, R. Shimon, Z.-Y. Lu, I. Hod, *ACS Appl. Energy Mater.* **2019**, *2*, 2138; b) B. M. Hunter, W. Hieringer, J. R. Winkler, H. B. Gray, A. M. Müller, *Energy Environ. Sci.* **2016**, *9*, 1734.
- [13] a) Z. Chen, Y. Ha, H. Jia, X. Yan, M. Chen, M. Liu, R. Wu, *Adv. Energy Mater.* **2019**, *9*, 1803918; b) Y. Zhang, H. Sun, Y. Qiu, X. Ji, T. Ma, F. Gao, Z. Ma, B. Zhang, P. Hu, *Carbon* **2019**, *144*, 370.
- [14] a) N. Cheng, L. Ren, X. Xu, Y. Du, S. X. Dou, *Adv. Energy Mater.* **2018**, *8*, 1801257; b) B. Chen, Z. Yang, Y. Zhu, Y. Xia, *J. Mater. Chem. A* **2014**, *2*, 16811.
- [15] S. Jiang, R. Zhang, H. Liu, Y. Rao, Y. Yu, S. Chen, Q. Yue, Y. Zhang, Y. Kang, *J. Am. Chem. Soc.* **2020**, *142*, 6461.
- [16] J.-H. Kim, K. Shin, K. Kawashima, D. H. Youn, J. Lin, T. E. Hong, Y. Liu, B. R. Wygant, J. Wang, G. Henkelman, C. B. Mullins, *ACS Catal.* **2018**, *8*, 4257.
- [17] H. Xu, J. Cao, C. Shan, B. Wang, P. Xi, W. Liu, Y. Tang, *Angew. Chem., Int. Ed.* **2018**, *57*, 8654.
- [18] a) H. Xu, Y. Yang, X. Yang, J. Cao, W. Liu, Y. Tang, *J. Mater. Chem. A* **2019**, *7*, 8284; b) X. Wu, Y. Yang, T. Zhang, B. Wang, H. Xu, X. Yan, Y. Tang, *ACS Appl. Mater. Interfaces* **2019**, *11*, 39841.
- [19] H. Xu, C. Shan, X. Wu, M. Sun, B. Huang, Y. Tang, C.-H. Yan, *Energy Environ. Sci.* **2020**, *13*, 2949.
- [20] J.-X. Feng, S.-H. Ye, H. Xu, Y.-X. Tong, G.-R. Li, *Adv. Mater.* **2016**, *28*, 4698.
- [21] M. Li, X. Pan, M. Jiang, Y. Zhang, Y. Tang, G. Fu, *Chem. Eng. J.* **2020**, *395*, 125160.
- [22] a) T. Zhang, X. Wu, Y. Fan, C. Shan, B. Wang, H. Xu, Y. Tang, *Chem-NanoMat* **2020**, *6*, 1119; b) X. Ren, F. Hou, F. Wang, X. Zhang, Q. Wang, *Int. J. Hydrogen Energy* **2018**, *43*, 22529.
- [23] F. Liang, Y. Yu, W. Zhou, X. Xu, Z. Zhu, *J. Mater. Chem. A* **2015**, *3*, 634.
- [24] W. Zheng, M. Liu, L. Y. S. Lee, *ACS Catal.* **2020**, *10*, 81.
- [25] H. Chu, D. Zhang, B. Jin, M. Yang, *Appl. Catal., B* **2019**, *255*, 117744.
- [26] a) S. Dou, L. Tao, J. Huo, S. Wang, L. Dai, *Energy Environ. Sci.* **2016**, *9*, 1320; b) H. Zou, G. Li, L. Duan, Z. Kou, J. Wang, *Appl. Catal., B* **2019**, *259*, 118100; c) Z.-H. Sheng, L. Shao, J.-J. Chen, W.-J. Bao, F.-B. Wang, X.-H. Xia, *ACS Nano* **2011**, *5*, 4350.
- [27] a) J. Haber, L. Ungier, *J. Electron Spectrosc. Relat. Phenom.* **1977**, *12*, 305; b) Y. Liu, C. Ma, Q. Zhang, W. Wang, P. Pan, L. Gu, D. Xu, J. Bao, Z. Dai, *Adv. Mater.* **2019**, *31*, 1900062.
- [28] a) W. He, R. Ifraemov, A. Raslin, I. Hod, *Adv. Funct. Mater.* **2018**, *28*, 1707244; b) N. Kornienko, J. Resasco, N. Becknell, C.-M. Jiang, Y.-S. Liu, K. Nie, X. Sun, J. Guo, S. R. Leone, P. Yang, *J. Am. Chem. Soc.* **2015**, *137*, 7448.
- [29] a) B. S. Yeo, A. T. Bell, *J. Am. Chem. Soc.* **2011**, *133*, 5587; b) J. Yang, H. Liu, W. N. Martens, R. L. Frost, *J. Phys. Chem. C* **2010**, *114*, 111.